The Astrophysical Journal, 832:191 (9pp), 2016 December 1 doi:10.3847/0004-637X/832/2/191


# VLT FORS2 COMPARATIVE TRANSMISSION SPECTROSCOPY: DETECTION OF Na IN THE ATMOSPHERE OF WASP-39b FROM THE GROUND

Nikolay Nikolov[1], David K. Sing[1], Neale P. Gibson[2], Jonathan J. Fortney[3], Thomas M. Evans[1], Joanna K. Barstow[4], Tiffany Kataria[5], and Paul A. Wilson[6]
[1] Physics and Astronomy, University of Exeter, EX4 4QL Exeter, UK; nikolay@astro.ex.ac.uk
[2] Astrophysics Research Centre, School of Mathematics and Physics, Queens University Belfast, Belfast BT7 1NN, UK
[3] Department of Astronomy and Astrophysics, University of California, Santa Cruz, CA 95064, USA
[4] Physics and Astronomy, University College London, London, UK
[5] Jet Propulsion Laboratory, California Institute of Technology, 4800 Oak Grove Drive, Pasadena, CA, USA
[6] Institut d'Astrophysique de Paris, UMR7095 CNRS, Université Pierre & Marie Curie, 98bis Boulevard Arago, 75014 Paris, France
*Received 2016 June 22; revised 2016 October 1; accepted 2016 October 3; published 2016 December 1*

## ABSTRACT

We present transmission spectroscopy of the warm Saturn-mass exoplanet WASP-39b made with the Very Large Telescope FOcal Reducer and Spectrograph (FORS2) across the wavelength range 411–810 nm. The transit depth is measured with a typical precision of 240 parts per million (ppm) in wavelength bins of 10 nm on a $V = 12.1$ mag star. We detect the sodium absorption feature ($3.2\sigma$) and find evidence of potassium. The ground-based transmission spectrum is consistent with *Hubble Space Telescope* (*HST*) optical spectroscopy, supporting the interpretation that WASP-39b has a largely clear atmosphere. Our results demonstrate the great potential of the recently upgraded FORS2 spectrograph for optical transmission spectroscopy, with which we obtained *HST*-quality light curves from the ground.

*Key words:* planets and satellites: atmospheres – stars: individual (WASP-39) – techniques: photometric – techniques: spectroscopic

## 1. INTRODUCTION

Transmission spectroscopy is a key to unlocking the secrets of close-in exoplanet atmospheres. Observations have started to unveil a vast diversity of irradiated giant planet atmospheres with clouds and hazes that play a prominent role across the entire mass and temperature regime (Charbonneau et al. 2002; Pont et al. 2008; Knutson et al. 2014; Kreidberg et al. 2014; Evans et al. 2016; Sing et al. 2016). Observations from space have played a leading role in the field, followed by significant achievements from the ground with the first results from multi-object (Bean et al. 2010; Crossfield et al. 2013; Gibson et al. 2013a; Jordán et al. 2013; Stevenson et al. 2014) and long-slit spectroscopy (Sing et al. 2012).

Ground-based spectrographs, which operate at medium resolution, have a high potential for characterizing transiting exoplanets because they provide optical transmission spectra that are highly complementary to the near- and mid-IR regime, which is to be covered by the upcoming *James-Webb Space Telescope*. The FOcal Reducer and Spectrograph (FORS2, Appenzeller et al. 1998) mounted on the Very Large Telescope (VLT) at the European Southern Observatory (ESO) has recently undergone an upgrade with the aim to improve its capability for exoplanet transmission spectroscopy (Boffin et al. 2015). Sedaghati et al. (2015) have recently presented observations of WASP-19b with the upgraded FORS2 instrument, but found a featureless flat transmission spectrum.

We have initiated a ground-based multi-object transmission spectroscopy of WASP-6b, WASP-31b, and WASP-39b that covers the wavelength range 360–850 nm using VLT FORS2. These targets were selected for follow-up as their transmission spectra showed evidence of alkali metal absorption based on the results of *Hubble Space Telescope* (*HST*) observations (Nikolov et al. 2015; Sing et al. 2015; Fischer et al. 2016). Our aim is to test the performance of FORS2, following its recent recommissioning (Sedaghati et al. 2015), by comparing the transmission spectra against results from the *HST*.

In this paper we report the first results from our comparative study for WASP-39b. This warm Saturn is one of the most favorable exoplanets for transmission spectroscopy (Faedi et al. 2011) with a pressure scale height of $H > 1000$ km, translating into an atmospheric signal of $\Delta\delta = 455$ ppm (Winn 2010). The recent *HST* results reported by Sing et al. (2016) and Fischer et al. (2016) show agreement with model spectra of a clear atmosphere and evidence of absorption from sodium and potassium, which makes WASP-39b an excellent target for ground-based optical transmission spectroscopy.

## 2. OBSERVATIONS

Time series observations were carried out during two primary transits of WASP-39b on UT 2016 March 8 and 12 with the FORS2 spectrograph mounted on the UT1 telescope at the European Southern Observatory on Cerro Paranal in Chile for program 096.C-0765 (PI: Nikolov). Data were collected in multi-object spectroscopy mode at medium resolution with a mask consisting of two broad slits centered on WASP-39 and one nearby reference star (known as 2MASS 14292245-0321010) at an angular separation of $\sim 5\farcm7$. The slits had lengths of $\sim 90''$ and widths of $22''$ to eliminate possible differential slit light losses from guiding imperfections and seeing variations. Both observations were performed with the same slit mask and the red detector, which is a mosaic of two CCDs. The field of view was positioned such that each individual chip imaged the spectrum of one star. To improve the duty cycle, the fastest available readout mode (~30 s) was employed.

During the first night we used the dispersive element GRIS600B, which covers the spectral range from 360 to 620 nm at a resolving power of $R \sim 600$. We monitored

WASP-39 and the reference star ($B$ magnitude difference of $-0.97$) for 312 minutes under photometric conditions. The field of view rose from an air mass of 1.89 to 1.07 and set to an airmass of 1.16. The seeing gradually increased, with median values from 0.7 to 1.8″ in the course of the observation, as measured from the spectra cross-dispersion profiles. A total of 216 exposures were collected with an integration time of 60 s.

During the second night we exploited the dispersive element GRIS600RI, which covers the range from 540 to 820 nm, in combination with the GG435 filter to isolate the first order. Both sources ($R$ magnitude difference of $-1.26$) were observed for 304 minutes under photometric sky conditions and increasing seeing, with a median value of 0.9–2.3″. The field of view rose from an air mass of 1.53 to 1.07 and set to an air mass of 1.23. A telescope guiding error at UT 4:45 prevented data collection for ∼5 minutes (during transit egress). A total of 232 exposures were collected with an integration time of 50 s.

## 3. DATA REDUCTIONS

Our analysis commenced from the raw images with subtraction of bias frame and flat field correction. The relevant master calibration frames were calculated by median-combining 100 individual frames. Spectral extractions were performed in IRAF, employing the APALL procedure. The background was estimated by taking the median count level in a box of pixels away from the spectral trace, and was subtracted from the stellar counts for each wavelength. We found that the aperture diameters of 24 and 30 pixels and a sky region from 40 to 70 pixels minimize the dispersion of the out-of-transit flux of the corresponding white-light curves for the first and second night, respectively.

Wavelength calibration of the extracted stellar spectra was performed using spectra of an emission lamp obtained after each transit observation with a mask identical to the science mask, but with slit widths of 1″. A wavelength solution was established for each source with a low-order Chebyshev polynomial fit to the centers of a dozen lines, the positions of which were determined with a Gaussian fit. We then placed the extracted spectra on a common Doppler-corrected rest frame through cross-correlation to account for subpixel wavelength shifts in the dispersion direction. We found a displacement range of the spectra $<3$ pixels during each observation; the gravity flexure of the instrument is the most likely reason for this.

Example spectra of WASP-39 and the reference star are displayed in Figure 1. The typical signal-to-noise ratio (S/N) achieved for WASP-39 and the reference star were 267 and 160 per pixel for the central wavelength of GRIS600B and 326 and 191 per pixel for the central wavelength of GRIS600RI. The one-dimensional spectra were then used to generate both white-light and spectrophotometric time series after summing the flux from each bandpass.

## 4. LIGHT CURVE ANALYSIS

White and spectroscopic light curves were created from the time series of each night for both the target and reference star by summing the flux of each stellar spectrum along the dispersion axis. Spectroscopic light curves were produced by adopting the set of bands defined in Sing et al. (2016) to enable a direct comparison with the *HST* transmission spectrum of WASP-39b. White-light curves were computed from 440 to 607 nm and from 540 to 810 nm for the first and second night, respectively. The range from 360 to 440 nm of GRIS600B was discarded in the white-light curve analysis because the S/N was insufficient owing to the low sensitivity of the red detector in that spectral region. Relative differential light curves were produced for the white-light and spectroscopic light curves by dividing the WASP-39 flux by the reference star flux. This correction removes the effects of atmospheric transparency variations, as demonstrated in Figure 1. The light curve from the second night showed a decrease in flux by between ∼30 minutes before and ∼80 minutes after the mid-transit. The exact cause of this effect is unknown, but it is most likely related to the vignetting of the field of view.

We fit each transit light curve with a two-component function that simultaneously models the transit and systematic effects. To model the transits, we adopted the complete analytic function given in Mandel & Agol (2002), which is parametrized with the mid-transit times ($T_{\rm mid}$), orbital period ($P$) and inclination ($i$), normalized planet semimajor axis ($a/R_*$), and planet-to-star radius ratio ($R_{\rm p}/R_*$).

Stellar limb-darkening was accounted for by adopting the two-parameter quadratic law with coefficients $u_1$ and $u_2$, computed using a three-dimensional stellar atmosphere model grid (Magic et al. 2015), adopting the closest match to the effective temperature, surface gravity, and metallicity of WASP-39 that were found in Faedi et al. (2011). Our choice for the limb-darkening law was motivated by the recent study of Espinoza & Jordán (2016), where the quadratic law has been demonstrated to introduce a negligible bias on the derived transit parameters for transiting systems similar to WASP-39. The quadratic limb-darkening law has also been extensively used in previous multi-object spectroscopy characterization studies of transiting exoplanets, e.g., Bean et al. (2010), Gibson et al. (2013a, 2013b), Stevenson et al. (2014, 2016), Jordán et al. (2013), Mallonn et al. (2015), Mallonn & Strassmeier (2016), and Nortmann et al. (2016). Theoretical limb-darkening coefficients were obtained by fitting the limb-darkened intensities of the three-dimensional models multiplied by the throughput profiles of GRIS600B and GRIS600RI (Sing 2010).

To account for systematics, we used a low-order polynomial (up to second degree with no cross terms) of air mass, spectral shift (displacement of the stellar spectra in the dispersion axis, as described in Section 3), average FWHM, the vertical position of the center of the spectrum of each channel, time, and the rate of change of the rotator angle. We then generated systematics models that spanned all possible combinations of detrending variables and performed separate fits using each systematics model included in the two-component function. The Akaike information criterion (AIC; Akaike 1974) was calculated for each attempted function and used to marginalize over the entire set of functions following Gibson (2014). Our choice to rely on the AIC instead of the Bayesian information criterion (BIC; Schwarz 1978) was determined by the fact that the BIC is more biased toward simple models than the AIC. The AIC therefore provides a more conservative model for the systematics and typically results in larger or more conservative error estimates, as demonstrated by Gibson (2014). Marginalization over multiple systematics models assumes equal prior weights for each model tested. This is a sensible assumption for simple polynomial expansions of basis inputs; however, the

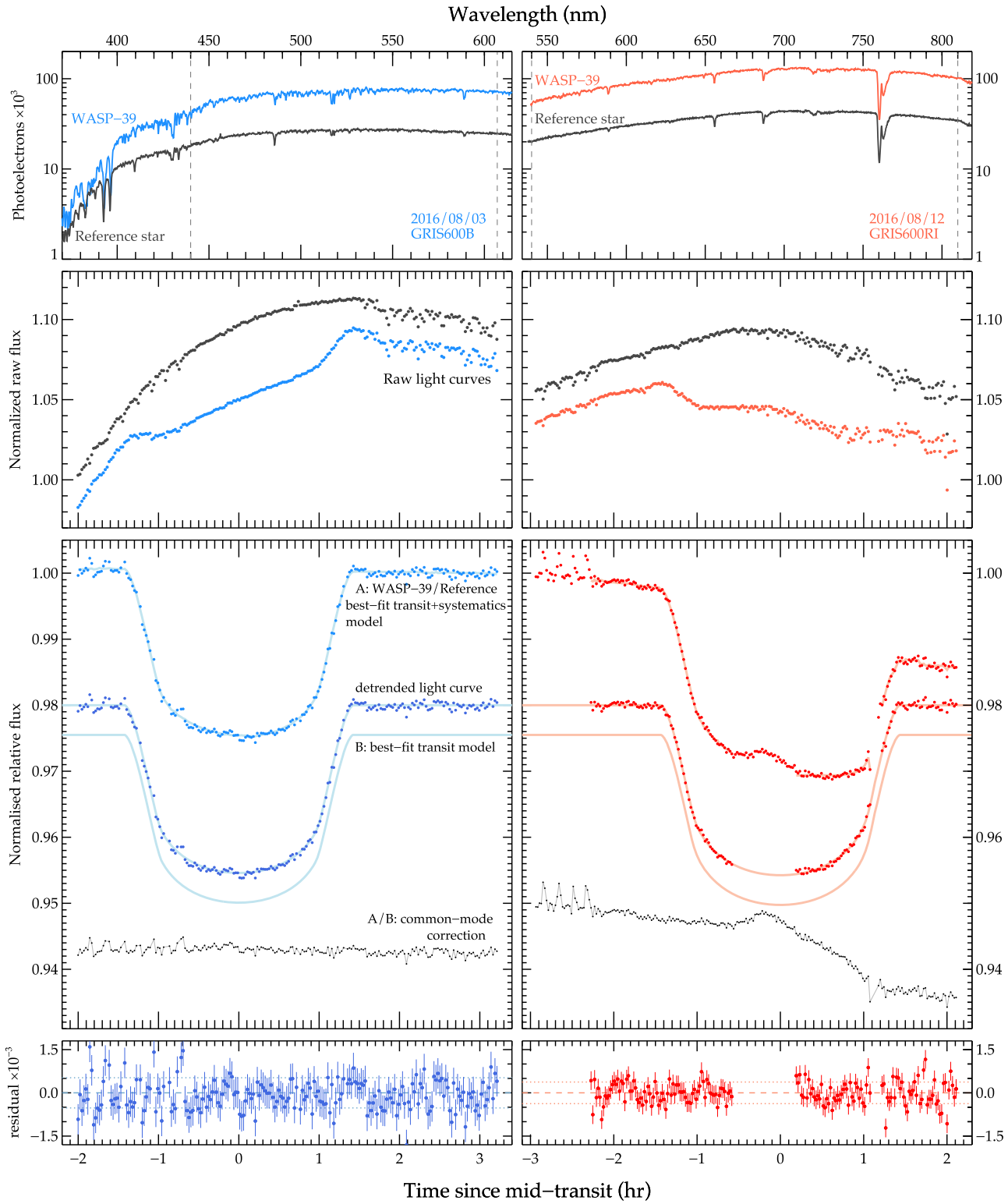


**Figure 1.** VLT FORS2 stellar spectra and the corresponding white-light transit light curves for WASP-39b and the reference star. Left and right column panels show the GRIS600B (blue) and GRIS600RI (red) data sets, respectively. First row: example stellar spectra used for relative spectrophotometric calibration. The dashed line indicates the wavelength range used to produce the white-light curves. Second row: raw light curves of both sources. Third row: WASP-39 light curve relative to the reference star with the best-fit transit and systematics model (A), detrended light curve along with the best-fit transit model (B), and common-mode correction (A/B). Fourth row: residual flux of the best-fit transit and systematics model to WASP-39.

introduction of more complex functional forms of the inputs (e.g., exponentials, sinusoids) would break the symmetry of the models and weaken this assumption when using simple model selection criteria such as the AIC.

The errors on each spectrophotometric data point from each time series were initially set to the pipeline values, which are dominated by photon noise, with readout noise also taken into account. We determined the best-fitting parameters

**Table 1**
System Parameters

| Parameter | Value |
|---|---|
| $P$(day) | 4.055259 (adopted) |
| $e$ | 0 (adopted) |
| *GRIS600B* | |
| $T_{\rm mid}$ (MJD) | 57455.26602 ± 0.00013 |
| $i$, (°) | 87.64 ± 0.17 |
| $a/R_*$ | 11.42 ± 0.17 |
| $R_{\rm p}/R_*$ | 0.1477 ± 0.0013 |
| $u_1$ | 0.433 ± 0.032 |
| $u_2$ | 0.27 |
| *GRIS600RI* | |
| $T_{\rm mid}$ (MJD) | 57459.32103 ± 0.00021 |
| $i$, (°) | 88.07 ± 0.23 |
| $a/R_*$ | 11.64 ± 0.15 |
| $R_{\rm p}/R_*$ | 0.1457 ± 0.0013 |
| $u_1$ | 0.485 ± 0.065 |
| $u_2$ | 0.30 |
| *Weighted mean:* | |
| $i$, (°) | 87.79 ± 0.14 |
| $a/R_*$ | 11.54 ± 0.11 |
| $R_{\rm p}/R_*$, GRIS600B | 0.14696 ± 0.00062 |
| $R_{\rm p}/R_*$, GRIS600RI | 0.14600 ± 0.00084 |

simultaneously with the Levenberg–Marquardt least-squares algorithm as implemented in the MPFIT[7] package of Markwardt (2009) using the unbinned data. The final results for the uncertainties of the fitted parameters were taken from MPFIT after we rescaled the errors per data point based on the standard deviation of the residuals. Residual outliers larger than $3\sigma$ (typically a few) were clipped in all light curves and the final results obtained with a fit performed using the rest of the data.

When fitting the white-light curve from the second night, we excluded data points from the first ∼40 minutes (because of the higher noise) and those exhibiting the flux drop as detailed in Section 3. We modeled each of the three remaining pieces of the light curve with individual systematics models and a common transit model. We found an excellent agreement between the fitted transit parameters from the two nights (Table 1).

For the spectroscopic light curves, a common-mode systematics model was established by simply dividing the white-light transit light curve to a transit model (Sing et al. 2012; Deming et al. 2013; Gibson et al. 2013a, 2013b; Huitson et al. 2013; Nikolov et al. 2015). We computed the transit model using the weighted mean values of the orbital inclination and $a/R_*$ from both observations. To find the best-fit radius and limb-darkening coefficients for the white-light curves, we fitted for these quantities, but fixed the remaining parameters to the weighted mean values, and the measured white-light transit depths are reported in Table 1.

We found systematics models containing an air mass, spectral shift, and FWHM terms to result in the highest evidence for the white-light curves. Following Pont et al. (2006), we assessed the levels of residual red noise by modeling the binned variance with a $\sigma^2 = (\sigma_w)^2/N + (\sigma_r)^2$ relation, where $\sigma_w$ is the uncorrelated white noise component, $N$ is the number points in the bin, and $\sigma_r$ characterizes the red noise. Typical white and red noise dispersions were found to be $\sigma_w \sim 540$ and ∼410 and $\sigma_r \sim 105$ and ∼100 ppm. The weighted mean values and radii found in the white-light curve analysis are in excellent agreement with the results of Sing et al. (2016) and Fischer et al. (2016).

The common-mode technique relies on the similarities of time-dependent systematics, which can be characterized by the light curves themselves and removed individually for each spectral wavelength bin. Empirically determining and removing slit light losses has an advantage over a parameterized method, as higher order frequencies are naturally subtracted. The common-mode factors from each night were then removed from the corresponding spectroscopic light curves before model fitting (see Figure 1).

We then performed fits to the spectroscopic light curves using the same set of systematics models as in the white-light curve analysis and marginalized over them as described above. For these fits, $R_{\rm p}/R_*$ and the first limb-darkening coefficient $u_1$ were allowed to vary for each spectroscopic channel, while the central transit time and system parameters were fixed to the weighted mean values. Again, the same quadratic limb-darkening law was used with the nonlinear coefficient fixed to its theoretical value, determined in the same way as for the white-light curve, and $u_1$ was allowed to vary. We performed tests by fitting only the first or second coefficient and fixing the other to its theoretical value; we found no difference in the resulting transmission spectrum. Fitting for the linear limb-darkening coefficient is a practice introduced by Southworth (2008). This practice has been demonstrated to generally perform well. Ground-based multi-object spectroscopy studies have also implemented this method, e.g., Stevenson et al. (2014, 2016), Mallonn et al. (2015), and Mallonn & Strassmeier (2016). We also fitted for both limb-darkening coefficients simultaneously and found that the uncertainty of the nonlinear coefficient is large. This implies that the quality of the light curves is insufficient for constraining the nonlinear coefficient. However, since the transmission spectrum did not significantly change, we chose to fix the nonlinear term to its theoretical prescription and fit for the linear term only. We report the results for $R_{\rm p}/R_*$ and the limb-darkening parameters in Table 2 and show the best-fit transit models in Figures 2 and 3. Much simpler systematics models were favored at the marginalization step for the spectroscopic light curves, typically containing only one term, e.g., linear airmass or a spectral shift term. In addition, we found that the spectroscopic light curves showed less scatter when flat fielding was not applied.

As checks of our reduction methods, we also performed a fit to the spectroscopic light curves without a common-mode correction and inflated the uncertainties with the $\beta$ scaling parameter. We also measured the radii for the blue grism by treating the systematics as a time-dependent Gaussian process (Gibson et al. 2012) without applying the common-mode correction; we found a consistent transmission spectrum. For the red grism the systematics are more complex and cannot be modeled using only time dependence. In all these checks we found the final transmission spectra to be in excellent agreement.

## 5. TRANSMISSION SPECTRUM

The measured VLT FORS2 transmission spectrum of WASP-39b is plotted in Figure 4. Its main characteristics

[7] http://www.physics.wisc.edu/craigm/idl/fitting.html

**Table 2**
Transmission Spectrum and Quadratic Limb-darkening Coefficients

| $\lambda$ (nm) | $R_p/R_*$ | $u_1$ | $u_2$ |
|---|---|---|---|
| 411–425 | 0.14673 ± 0.00255 | 0.612 ± 0.027 | 0.216 |
| 425–440 | 0.14578 ± 0.00170 | 0.669 ± 0.028 | 0.225 |
| 440–450 | 0.14648 ± 0.00139 | 0.546 ± 0.036 | 0.229 |
| 450–460 | 0.14454 ± 0.00135 | 0.574 ± 0.024 | 0.233 |
| 460–470 | 0.14554 ± 0.00122 | 0.572 ± 0.025 | 0.239 |
| 470–480 | 0.14459 ± 0.00089 | 0.517 ± 0.026 | 0.246 |
| 480–490 | 0.14449 ± 0.00106 | 0.478 ± 0.026 | 0.246 |
| 490–500 | 0.14560 ± 0.00111 | 0.484 ± 0.023 | 0.249 |
| 500–510 | 0.14453 ± 0.00109 | 0.464 ± 0.024 | 0.256 |
| 510–520 | 0.14403 ± 0.00096 | 0.380 ± 0.035 | 0.265 |
| 520–530 | 0.14339 ± 0.00198 | 0.446 ± 0.028 | 0.267 |
| 530–540 | 0.14501 ± 0.00099 | 0.394 ± 0.023 | 0.268 |
| 540–550 | 0.14523 ± 0.00112 | 0.412 ± 0.027 | 0.273 |
| 550–565 | 0.14617 ± 0.00096 | 0.397 ± 0.025 | 0.283 |
| 565–587 | 0.14641 ± 0.00067 | 0.310 ± 0.017 | 0.289 |
| 587–590 | 0.15026 ± 0.00206 | 0.228 ± 0.049 | 0.289 |
| 590–607 | 0.14634 ± 0.00078 | 0.305 ± 0.021 | 0.285 |
| 565–587 | 0.14479 ± 0.00114 | 0.348 ± 0.015 | 0.310 |
| 587–590 | 0.14951 ± 0.00214 | 0.352 ± 0.038 | 0.311 |
| 590–607 | 0.14389 ± 0.00130 | 0.385 ± 0.017 | 0.312 |
| 607–630 | 0.14516 ± 0.00070 | 0.351 ± 0.013 | 0.313 |
| 630–645 | 0.14440 ± 0.00088 | 0.331 ± 0.015 | 0.314 |
| 645–660 | 0.14520 ± 0.00113 | 0.329 ± 0.016 | 0.313 |
| 660–680 | 0.14446 ± 0.00120 | 0.324 ± 0.012 | 0.314 |
| 680–710 | 0.14414 ± 0.00067 | 0.327 ± 0.010 | 0.314 |
| 710–765 | 0.14459 ± 0.00145 | 0.323 ± 0.012 | 0.315 |
| 765–770 | 0.14742 ± 0.00130 | 0.300 ± 0.026 | 0.315 |
| 770–810 | 0.14643 ± 0.00090 | 0.309 ± 0.013 | 0.315 |

include sodium and potassium absorption features, spanning ~5 and ~3 atmospheric pressure scale heights, respectively, and a relatively flat baseline. Band 587–590 nm, which is centered on the sodium line core, shows larger absorption than the surrounding bands in each of the two separate epoch observations with GRIS600B and GRIS600RI. Comparing the pairs of radius measurements of our result to the spectrum of (Sing et al. 2016), we can find that all of the measurements are in agreement within their uncertainties. A least-squares fit with a constant being the only fitted parameter to the differences between the *HST* STIS and VLT FORS2 spectra, using the uncertainties combined in quadrature, gives $\chi^2$ of 38.68 for 27 degrees of freedom and an offset between the two spectra of $\Delta R_p/R_* = 0.00097 \pm 0.00043$. The probability of obtaining this $\chi^2$ value is ~7% and cannot reject a constant offset model; this implies that the spectra are consistent. It should be noted that the overall level of the VLT FORS2 transmission spectrum is as uncertain as the white-light curve depths for the two grisms (see Section 4), which accounts for common-mode corrections, and correlations with other transit parameters that are fixed for the spectroscopic fits. When we stitch multiple transit spectra together, we can ensure that the same system parameters are used, but we cannot correct for bias in various common-mode corrections.

To estimate the significance of the Na and K detection, we performed a horizontal line fit to the FORS2 transmission spectrum, excluding the measurements in the Na (2) and K (1) bins. We then computed the weighted mean value of the Na measurement and compared the difference of this measurement with the measurement from the horizontal line. When we repeated this for the Na and K lines, we found 3.2 and 1.7$\sigma$ confidence levels.

## 6. DISCUSSION

We compared the FORS2 transmission spectrum to a variety of different cloud-free atmospheric models based on the formalism of Fortney et al. (2008, 2010). We averaged the models within the transmission spectrum wavelength bins and fitted these theoretical values to the data with a single free parameter that controls their vertical position. We computed the $\chi^2$ statistics to quantify the model selection with the number of degrees of freedom for each model given by $\nu = N - m$, where $N$ is the number of data points and $m$ is the number of fitted parameters.

Results from the model comparison are shown in Figure 5. We find the cloud-free solar-metallicity models with an artificially added 1× uniform absorber from large particles (red line) and 10× Rayleigh scattering from small particles (blue line) to be the best-match to the 28 data points. The featureless models with 100× enhanced scattering from large particles (the horizontal brown line in Figure 5) and 1000× Rayleigh scattering (orange line) resulted in quite high values for the $\chi^2$-statistic and were disfavored.

We also performed a linear fit to the Rayleigh slope from 411 to 530 nm to empirically measure the temperature at the planet's day–night terminator. Assuming an atmospheric opacity source(s) with an effective extinction (scattering +absorption) cross-section that follows a power law of index $\alpha$, i.e., $\sigma = \sigma_0 (\lambda/\lambda_0)^{\alpha}$, the transmission spectrum is then proportional to the product $\alpha T$ given by

$$\alpha T = \frac{\mu g}{k} \frac{d (R_p/R_*)}{d \ln \lambda}. \quad (1)$$

where $\mu$ is the mean molecular mass, $g$ is the surface gravity, $k$ is the Boltzman constant, and $T$ is the temperature (Lecavelier Des Etangs et al. 2008). We found a good fit to the 12 FORS2 data points ($\chi^2 = 3.1$ for $\nu = 10$, $m = 2$) giving $\alpha T = -4795 \pm 3913$ K. For comparison, a horizontal line fit (cloud deck) resulted in a slightly poorer fit with $\chi^2 = 3.9$ for $\nu = 11$ and $m = 1$. When we adopt the equilibrium temperature from Faedi et al. 2011, the slope of the transmission suggests an effective extinction cross-section of $\sigma = \sigma_0 (\lambda/\lambda_0)^{-4.3 \pm 3.5}$, which is consistent with Rayleigh scattering.

When we assume Rayleigh scattering (i.e., adopting $\alpha = -4$), which is the case for a pure gaseous $H_2$ atmosphere or scattering, we find a best-fit terminator temperature of $1199 \pm 978$, which is in agreement with the result of Fischer et al. (2016).

The model comparison to our VLT observations demonstrates that scenarios including an atmosphere dominated by a cloud deck or strong Rayleigh scattering are ruled out. A clear atmosphere with clouds and hazes seems to be the most plausible scenario for WASP-39b, which is in agreement with the results from *HST* and *Spitzer*. This is in contrast to WASP-6b and HD 189733b, two other planets with equilibrium temperatures similar to WASP-39b (~1100 K) and measured optical transmission spectra that reveal hazy atmospheres.

Our results also demonstrate the capability and high potential of FORS2 to characterize exoplanets in transmission. We note that the efficiency and wavelength coverage of our observation

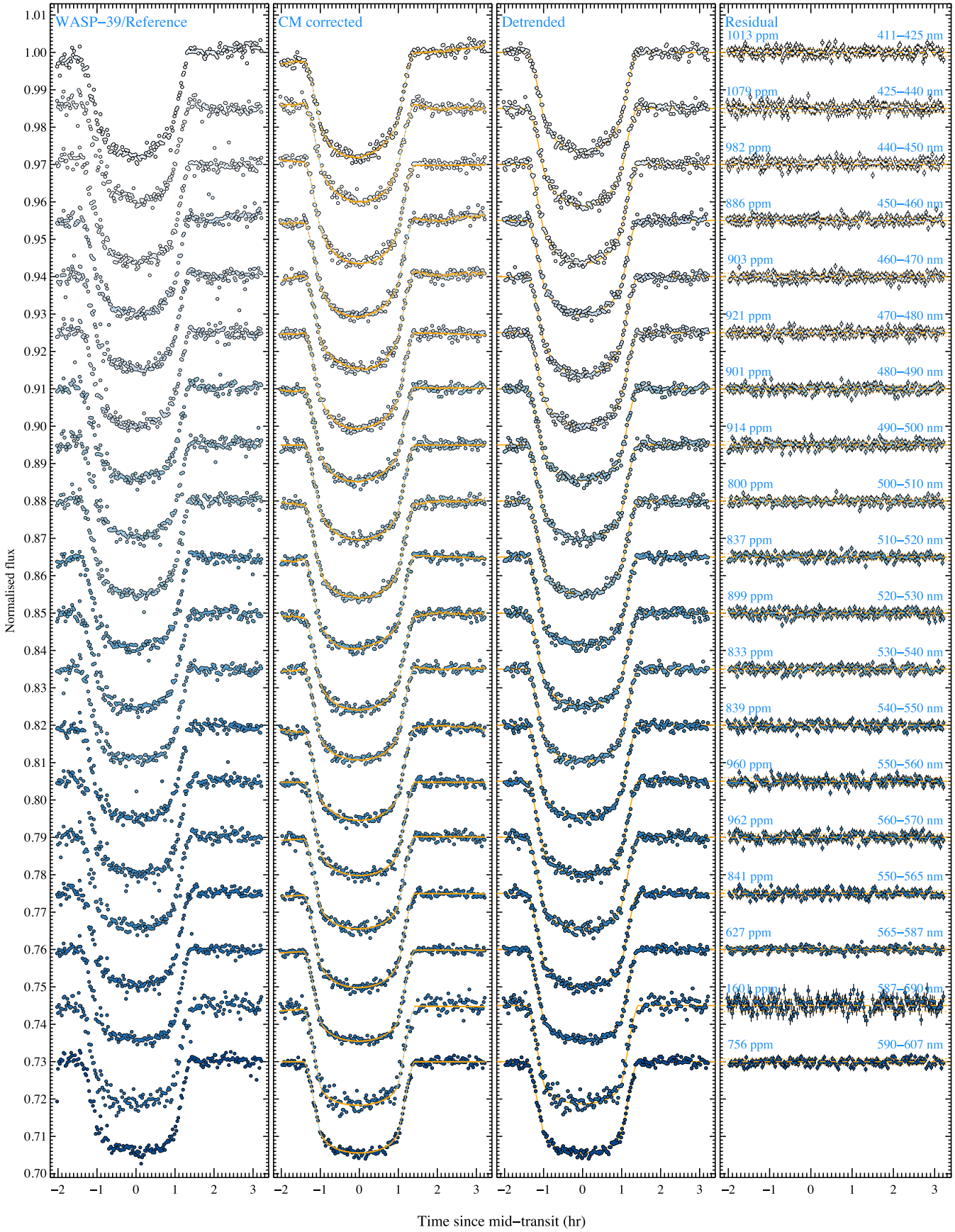


**Figure 2.** Spectroscopic light curves from GRIS600B offset by an arbitrary constant for clarity. First panel: raw target-to-reference flux. Second panel: common-mode corrected data and the best-fit model. Third panel: detrended light curves and the best-fit transit model. Fourth panel: residuals with $1\sigma$ error bars. The dashed lines show the median residual level, with dotted lines indicating the dispersion, which is also labeled for each channel.

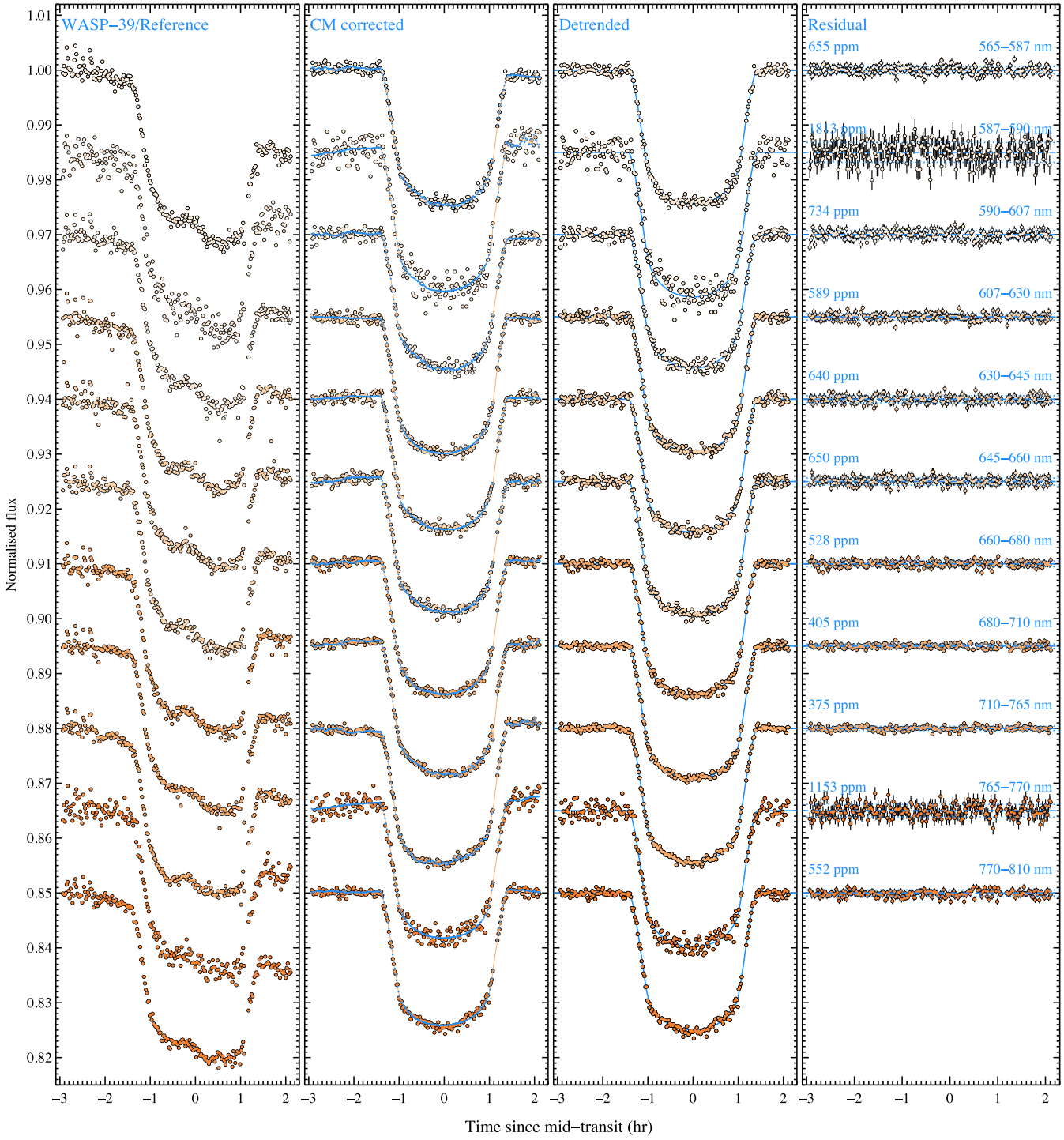


**Figure 3.** Same as Figure 2, but for GRIS600RI.

could further be increased by exploiting the blue rather than the red detector when using grism GRIS600B with an expected improvement of $\sim 2\times$ in S/N. This is especially pertinent to constraining the near-UV slope caused by molecular hydrogen and could provide constraints on the planet temperature and base pressure.

## 7. CONCLUSION

We report on a ground-based optical transmission spectrum for WASP-39b that covers the wavelength range from 411 to 810 nm and was obtained with the recently upgraded VLT FORS2 instrument, configured for multi-object spectroscopy. We detect an absorption from sodium ($\sim 3.2\sigma$) and find evidence of potassium ($\sim 1.7\sigma$). Our spectrum is consistent with the transmission spectrum obtained with the *HST* and further supports the finding of a largely clear atmosphere. Our study demonstrates the high potential of the instrument for optical transmission spectroscopy; it is capable of obtaining *HST*-quality light curves from the ground. Compared to *HST*, the larger aperture of VLT will allow for fainter targets to be

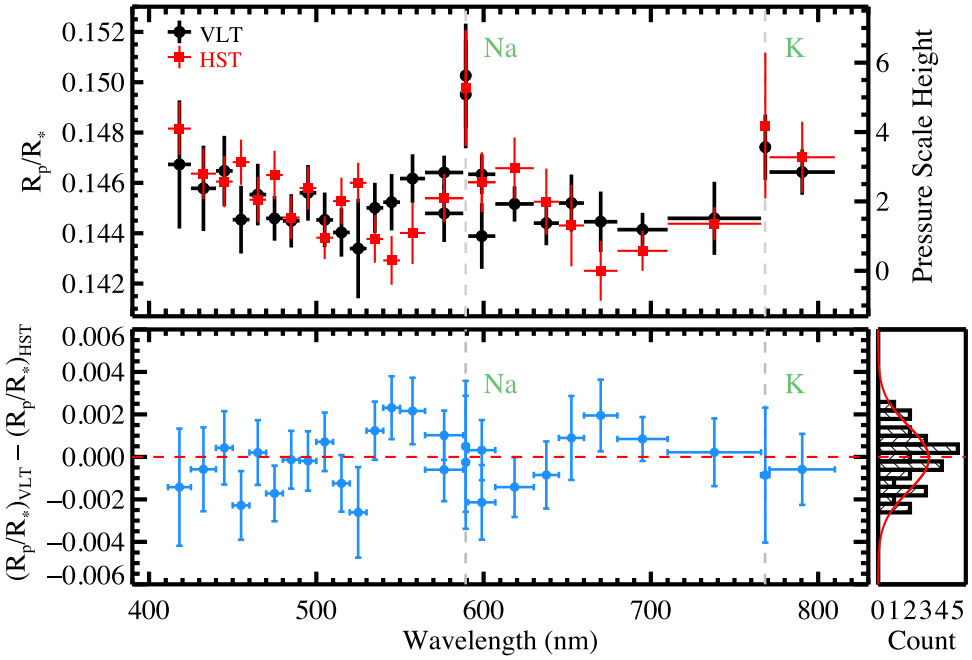


**Figure 4.** Comparison between the WASP-39b transmission spectrum from VLT FORS2 and *HST* STIS. The top panel displays the individual measurements with their uncertainties. The lower panels display the radius differences, assuming the uncertainty of the FORS2 and STIS measurements. The residual distribution is shown on the right along with the best-fit Gaussian, which is indicated with the red continuos line.

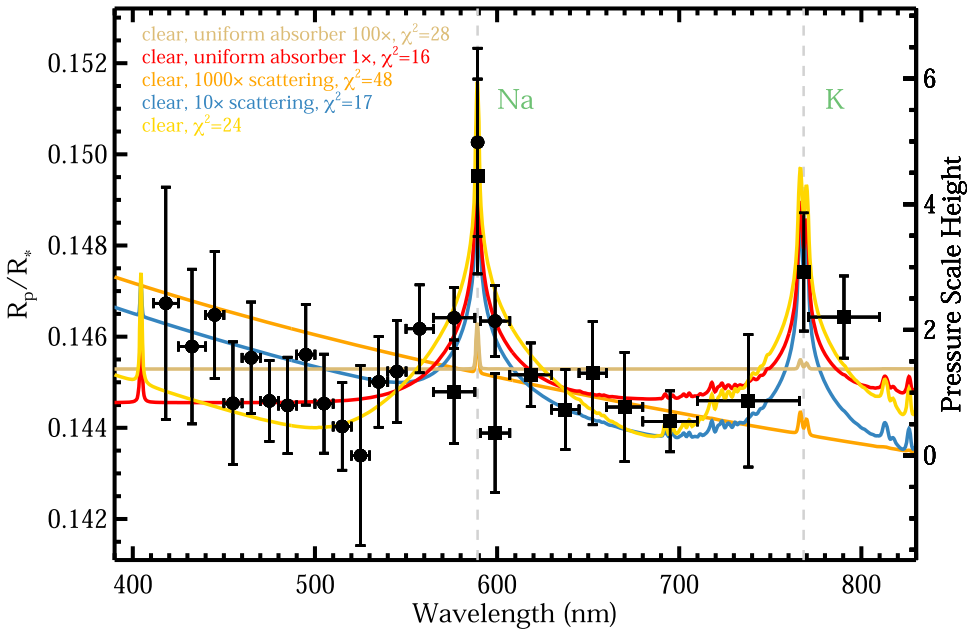


**Figure 5.** Comparison of the FORS2 transmission spectrum (dots and boxes refer to GRIS600B and GRIS600RI, respetively) to models (continuous lines).

observed and will achieve higher spectral resolution, which can greatly aid comparative exoplanet studies.

Based on observations collected at the European Organization for Astronomical Research in the Southern Hemisphere under ESO program 096.C-0765(E). We are grateful to the anonymous referee for their valuable comments and suggestions for improving the manuscript. The research leading to these results received funding from the European Research Council under the European Union Seventh Framework Program (FP7/2007-2013) ERC grant agreement no. 336792. N.P.G. gratefully acknowledges support from the Royal Society in the form of a University Research Fellowship. J.K. B. and E.R.C. acknowledge support from project 617119 (ExoLights). P.A.W. acknowledges the support of the French Agence Nationale de la Recherche (ANR), under program ANR-12-BS05-0012 "Exo-Atmos."

## REFERENCES

Akaike, H. 1974, ITAC, 19, 716
Appenzeller, I., Fricke, K., Fürtig, W., et al. 1998, Msngr, 94, 1
Bean, J. L., Désert, J.-M., Seifahrt, A., et al. 2013, ApJ, 771, 108
Bean, J. L., Miller-Ricci Kempton, E., & Homeier, D. 2010, Natur, 468, 669
Boffin, H., Blanchard, G., Gonzalez, O., et al. 2015, Msngr, 159, 6

Charbonneau, D., Brown, T. M., Noyes, R. W., & Gilliland, R. L. 2002, ApJ, 568, 377
Crossfield, I. J. M., Barman, T., Hansen, B. M. S., & Howard, A. W. 2013, A&A, 559, A33
Deming, D., Wilkins, A., McCullough, P., et al. 2013, ApJ, 774, 95
Espinoza, N., & Jordán, A. 2016, MNRAS, 457, 3573
Espinoza, N., & Jordán, A. 2016, MNRAS, 457, 3573
Evans, T. M., Sing, D. K., Wakeford, H. R., et al. 2016, ApJL, 822, L4
Faedi, F., Barros, S. C. C., Anderson, D. R., et al. 2011, A&A, 531, A40
Fischer, P. D., Knutson, H. A., Sing, D. K., et al. 2016, ApJ, 827, 19
Fortney, J. J., Lodders, K., Marley, M. S., & Freedman, R. S. 2008, APJ, 678, 1419
Fortney, J. J., Shabram, M., Showman, A. P., et al. 2010, ApJ, 709, 1396
Gibson, N. P. 2014, MNRAS, 445, 3401
Gibson, N. P., Aigrain, S., Barstow, J. K., et al. 2013a, MNRAS, 428, 3680
Gibson, N. P., Aigrain, S., Barstow, J. K., et al. 2013b, MNRAS, 436, 2974
Gibson, N. P., Aigrain, S., Roberts, S., et al. 2012, MNRAS, 419, 2683
Huitson, C. M., Sing, D. K., Pont, F., et al. 2013, MNRAS, 434, 3252
Huitson, C. M., Sing, D. K., Vidal-Madjar, A., et al. 2012, MNRAS, 422, 2477
Jordán, A., Espinoza, N., Rabus, M., et al. 2013, ApJ, 778, 184
Knutson, H. A., Dragomir, D., Kreidberg, L., et al. 2014, ApJ, 794, 155
Kreidberg, L., Bean, J. L., Désert, J.-M., et al. 2014, Natur, 505, 69
Lecavelier Des Etangs, A., Pont, F., Vidal-Madjar, A., & Sing, D. 2008, A&A, 481, L83
Magic, Z., Chiavassa, A., Collet, R., & Asplund, M. 2015, A&A, 573, A90
Mallonn, M., & Strassmeier, K. G. 2016, A&A, 590, A100
Mallonn, M., von Essen, C., Weingrill, J., et al. 2015, A&A, 580, A60
Mandel, K., & Agol, E. 2002, ApJL, 580, L171
Markwardt, C. B. 2009, adass XVIII, 411, 251
Nikolov, N., Sing, D. K., Burrows, A. S., et al. 2015, MNRAS, 447, 463
Nikolov, N., Sing, D. K., Pont, F., et al. 2014, MNRAS, 437, 46
Nortmann, L., Palle, E., Murgas, F., et al. 2016, A&A, 594, A65
Pont, F., Knutson, H., Gilliland, R. L., Moutou, C., & Charbonneau, D. 2008, MNRAS, 385, 109
Pont, F., Zucker, S., & Queloz, D. 2006, MNRAS, 373, 231
Redfield, S., Endl, M., Cochran, W. D., & Koesterke, L. 2008, ApJL, 673, L87
Schwarz, G. 1978, AnSta, 6, 461
Sedaghati, E., Boffin, H. M. J., Csizmadia, S., et al. 2015, A&A, 576, L11
Sing, D. K. 2010, A&A, 510, A21
Sing, D. K., Fortney, J. J., Nikolov, N., et al. 2016, Natur, 529, 59
Sing, D. K., Huitson, C. M., Lopez-Morales, M., et al. 2012, MNRAS, 426, 1663
Sing, D. K., Wakeford, H. R., Showman, A. P., et al. 2015, MNRAS, 446, 2428
Snellen, I. A. G., Albrecht, S., de Mooij, E. J. W., & Le Poole, R. S. 2008, A&A, 487, 357
Southworth, J. 2008, MNRAS, 386, 1644
Stevenson, K. B., Bean, J. L., Madhusudhan, N., & Harrington, J. 2014, ApJ, 791, 36
Stevenson, K. B., Bean, J. L., Seifahrt, A., et al. 2016, ApJ, 817, 141
Winn, J. N. 2010, arXiv:1001.2010